NAVAL POSTGRADUATE SCHOOL

MONTEREY, CALIFORNIA

THESIS

PERFORMANCE ANALYSIS OF DIRECTION OF ARRIVAL ESTIMATION FOR A 3-D UNIFORM VOLUME ARRAY

by

Kenneth A. Fletcher II

June 2021

Thesis Advisor: Ric Romero
Co-Advisor: David C. Jenn

THIS PAGE INTENTIONALLY LEFT BLANK

REPORT DOCUMENTATION PAGE	*Form Approved OMB No. 0704-0188*

1. AGENCY USE ONLY *(Leave blank)*	**2. REPORT DATE** June 2021	**3. REPORT TYPE AND DATES COVERED** Master's thesis

4. TITLE AND SUBTITLE
PERFORMANCE ANALYSIS OF DIRECTION OF ARRIVAL ESTIMATION FOR A 3-D UNIFORM VOLUME ARRAY

5. FUNDING NUMBERS

6. AUTHOR(S) Kenneth A. Fletcher II

7. PERFORMING ORGANIZATION NAME(S) AND ADDRESS(ES)
Naval Postgraduate School
Monterey, CA 93943-5000

8. PERFORMING ORGANIZATION REPORT NUMBER

9. SPONSORING / MONITORING AGENCY NAME(S) AND ADDRESS(ES)
N/A

10. SPONSORING / MONITORING AGENCY REPORT NUMBER

11. SUPPLEMENTARY NOTES The views expressed in this thesis are those of the author and do not reflect the official policy or position of the Department of Defense or the U.S. Government.

12a. DISTRIBUTION / AVAILABILITY STATEMENT
Approved for public release. Distribution is unlimited.

12b. DISTRIBUTION CODE
A

13. ABSTRACT (maximum 200 words)

In this thesis, performance analysis of direction of arrival estimation using an antenna array is performed. We apply methods and concepts commonly used in 1-d linear and 2-d planar arrays to create a 3-d isotropic, uniform volume array. We compare and contrast the effectiveness of a 1-d, 2-d, and 3-d uniform isotropic array to observe the advantages of each. We incorporate the effect of element factor when using half-wave dipole antenna elements rather than isotropic point sources for the elements in our array. We also consider the polarization of the incident wave impinging upon the array. We build three 3-d orthogonal arrays of colinear dipoles and evaluate their performance using two estimation techniques over varying angles of incidence and power levels. The estimation techniques utilized are the maximum likelihood estimation (MLE) and minimum variance distortionless response (MVDR), which are compared against the Cramér–Rao bound (CRB). Performance analysis of these arrays corresponding to the two estimation techniques is performed and summarized. The results show the benefits and limitations of a uniform 3-d antenna array over others.

14. SUBJECT TERMS direction finding, angle of arrival estimation, performance analysis, sensitivity analysis, 3-dimensional arrays, likelihood estimation, uniform antenna arrays	**15. NUMBER OF PAGES** 63
	16. PRICE CODE

17. SECURITY CLASSIFICATION OF REPORT	**18. SECURITY CLASSIFICATION OF THIS PAGE**	**19. SECURITY CLASSIFICATION OF ABSTRACT**	**20. LIMITATION OF ABSTRACT**
Unclassified	Unclassified	Unclassified	UU

NSN 7540-01-280-5500

Standard Form 298 (Rev. 2-89)
Prescribed by ANSI Std. 239-18

THIS PAGE INTENTIONALLY LEFT BLANK

Approved for public release. Distribution is unlimited.

PERFORMANCE ANALYSIS OF DIRECTION OF ARRIVAL ESTIMATION FOR A 3-D UNIFORM VOLUME ARRAY

Kenneth A. Fletcher II
Lieutenant, United States Navy
BSEE, University of Idaho, 2013

Submitted in partial fulfillment of the
requirements for the degree of

MASTER OF SCIENCE IN ELECTRICAL ENGINEERING

from the

NAVAL POSTGRADUATE SCHOOL
June 2021

Approved by: Ric Romero
Advisor

David C. Jenn
Co-Advisor

Douglas J. Fouts
Chair, Department of Electrical and Computer Engineering

THIS PAGE INTENTIONALLY LEFT BLANK

ABSTRACT

In this thesis, performance analysis of direction of arrival estimation using an antenna array is performed. We apply methods and concepts commonly used in 1-d linear and 2-d planar arrays to create a 3-d isotropic, uniform volume array. We compare and contrast the effectiveness of a 1-d, 2-d, and 3-d uniform isotropic array to observe the advantages of each. We incorporate the effect of element factor when using half-wave dipole antenna elements rather than isotropic point sources for the elements in our array. We also consider the polarization of the incident wave impinging upon the array. We build three 3-d orthogonal arrays of colinear dipoles and evaluate their performance using two estimation techniques over varying angles of incidence and power levels. The estimation techniques utilized are the maximum likelihood estimation (MLE) and minimum variance distortionless response (MVDR), which are compared against the Cramér–Rao bound (CRB). Performance analysis of these arrays corresponding to the two estimation techniques is performed and summarized. The results show the benefits and limitations of a uniform 3-d antenna array over others.

THIS PAGE INTENTIONALLY LEFT BLANK

Table of Contents

List of Figures

List of Tables

THIS PAGE INTENTIONALLY LEFT BLANK

List of Acronyms and Abbreviations

1-d	1-dimensional
2-d	2-dimensional
3-d	3-dimensional
AOA	angle of arrival
CRB	Cramér–Rao bound
dB	decibel
DF	direction finding
EW	electronic warfare
I	in-phase
K	number of snapshots
MLE	maximum likelihood estimation
MVDR	minimum variance distortionless response
NB	narrowband
Q	quadrature
SNR	signal-to-noise
WB	wideband

THIS PAGE INTENTIONALLY LEFT BLANK

Acknowledgments

I want to thank my wife, Ashley, for her unwavering support in every aspect of my education, career, and life. Acknowledgment is deserved to my dogs, Zephyr and Apollo, for providing me with a consistent and much-needed distraction from the rigors of electrical engineering.

My deepest gratitude to both Dr. Ric Romero and Dr. David Jenn for their consistent support throughout every aspect of my thesis. Without their constant input and support, none of this research would have been possible.

THIS PAGE INTENTIONALLY LEFT BLANK

CHAPTER 1:
Introduction

1.1 Direction Finding Estimation Introduction

In the modern era of antennas, there has been a great deal of work in the area of direction finding (DF) and parameter estimation. Ever since the first antenna models (dipoles, loops, etc.) were used to form an array of antennas [1], the concept of direction finding has greatly evolved with the advent of modern digital processing and simulation. Direction finding has applications in radar, astronomy, communications, sonar, seismology, medical applications, and many others [2]. The potential to track and monitor targets in real time over large geographical areas makes the applications for this area of study seemingly limitless.

1.2 Motivation

Numerous texts and papers discuss mature direction finding using uniform, isotropic antenna array models for both 1-d (1-dimensional) and 2-d (2-dimensional), including [1]–[9].

Although there have been studies in 3-d (3-dimensional) arrays, such as surface cylinders due to physical constraints [10], our goal here is to study a true volumetric array. Uniform linear and planar, isotropic arrays in 1-d and 2-d such as in [2], are a logical place to start our expansion into the realm of volumetric 3-d antenna arrays. From here, we can expand our model to a 3-d uniform, volumetric antenna array, as shown in Figure 1.1. Comparison of these three different uniform arrays will give some intuitive insight into the numerical advantage of a 3-d volumetric array over a 2-d planar array and 1-d linear array.

Moreover, replacing isotropic point sources with real elements (dipoles, loops, etc.) allows us to closely model and simulate how a 3-d antenna array would function practically with direction finding and parameter estimation, as shown in the model in Figure 1.2. Considering the actual element factors of a half-wave dipole, as well as taking into account the polarization of the incident wave upon the array, has significant impact upon the estimation techniques performed. Both of these concepts are crucial to the understanding of the simulation results as they would apply to physical implementation and application.

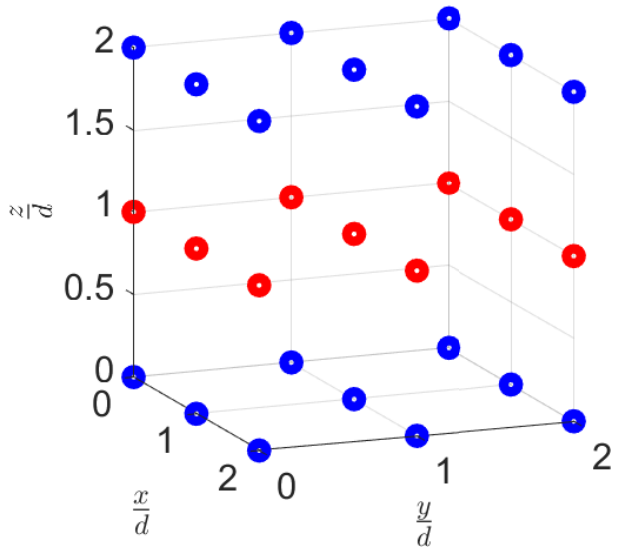

Figure 1.1. Isotropic, uniform volumetric array with 3 elements along x, y, and z axes spaced integer multiples of d apart.

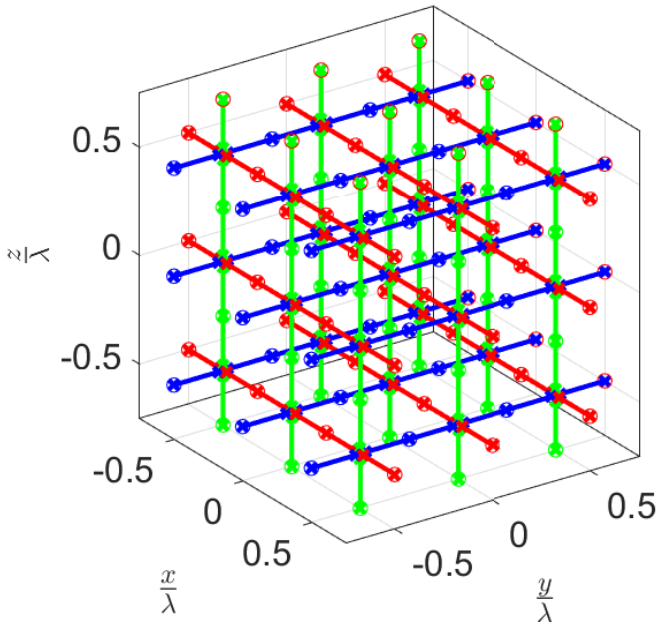

Figure 1.2. 3-d colinear dipole arrays, $N_x = N_y = N_z = 3$, where N is the number of elements per dimension spaced $\frac{\lambda}{2}$ apart, and centered at the origin.

Three-dimensional antenna arrays (as another dimension is added to 2-d) require significant computation and signal samples to accurately and precisely estimate the direction of arrival of a signal. One reason is due to the constraints and limitations of the maximum likelihood estimation (MLE) and minimum variance distortionless response (MVDR) estimation techniques, which will be discussed further. Additionally, we compare the performance of these estimation techniques against the standard of the Cramér–Rao bound (CRB) for each case to be examined, as in [1], [5], and [7].

1.3 Objective

One of our objectives in this thesis is to extend an accurate model for an isotropic, point-source uniform 1-d array to both 2-d and 3-d point-source uniform arrays. This allows us to create an accurate simulation of the 3-d dipole array and to evaluate its performance as a direction finding estimator, which will be compared with both 2-d and 1-d with the same number of antennas (N) in each direction (thus, N^2 for a 2-d square array, and N^3 for a 3-d cubic array).

From here, we can replace our isotropic point source antenna with a half-wave dipole antenna and compare the effectiveness of our 3-d antenna arrays. This is performed by considering the actual element factors of the colinear dipoles, which are based on their orientation in Cartesian space and the polarization of the incident wave [4]. This study gives insight to the numerical advantage of a true 3-d volume array over a 2-d planar array and evaluates the feasibility of constructing such an array using real half-wave dipole elements.

1.4 Thesis Organization

This thesis is organized as follows. In Chapter II, we describe the concept of an array manipulation vector that is used in our system model. This baseline concept is crucial to accurately simulating the antenna array model for our analysis. After we introduce the array manipulation vector in 1-d, we apply concepts of geometry and properties of matrices to expand our signal model to be manipulated in both 2-d and eventually 3-d. Additionally, we introduce the concept of the element factor and normalized array pattern to use with a half-wave dipole antenna model. In Chapter III, we discuss the application and limitations of our estimation techniques: MLE and MVDR. In Chapter III, we also present and explain

the basis for the CRB. In Chapter IV, we evaluate the effectiveness of the MLE and MVDR techniques by comparing the results against the CRB when applied to a uniform 1-d, 2-d, and 3-d antenna arrays. In Chapter V, the same performance analysis is conducted, but with 3-d antenna arrays using half-wave dipole elements of different orientation, to compare and contrast the effectiveness of each array estimate. In Chapter VI, we summarize our conclusions and propose possible future work in this area.

CHAPTER 2:
Development of 3-d Volumetric Antenna Array Model

2.1 The Array Manipulation Vector

2.1.1 The 1-D Array Manipulation Vector

Traditional antenna array models use the concept of the array manifold vector [1], array steering vector, or array manipulation vector [2]. It is worth noting that this signal concept has proven to be very useful and further discussion can be found in several sources such as [11], [12]. We assume a plane-wave signal impinging on the array of the form $s(t)e^{j\omega_c t}$, where $s(t)$ is the baseband signal and ω_c is of course equal to $2\pi f_c$ where f_c is the carrier frequency. For a uniform linear 1-d array, the signal received at one element of the array is just a delayed version from one adjacent to it.

Thus, the received signal (where $n = 0, 1, 2, ..., N-1$ is the element index) then becomes

$$\begin{bmatrix} s(t-\tau_0)e^{j\omega_c(t-\tau_1)} \\ s(t-\tau_1)e^{j\omega_c(t-\tau_2)} \\ . \\ . \\ . \\ s(t-\tau_{N-1})e^{j\omega_c(t-\tau_{N-1})} \end{bmatrix}, \tag{2.1}$$

where τ_n is the propagation delay of the n^{th} element of the array to a common reference point , e.g., $n = 0$ in our case [1]. In the case of the uniform linear array,

$$\tau_n = -\frac{d_x n}{c}\sin\theta, \tag{2.2}$$

where θ is measured from broadside. To avoid grating lobes, we let d_x be $\frac{\lambda}{2}$, where d_x is the space between elements along the x-axis shown in Figure 2.1.

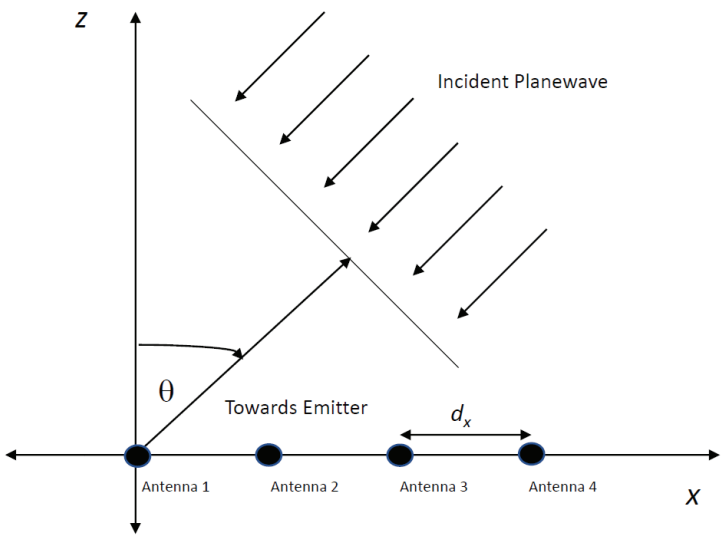

Figure 2.1. Isotropic, uniform linear array with four elements along x-axis.

In the case of the narrowband assumption, $B << f_c/L$, where B is the bandwidth and L is the length of the aperture in wavelengths. So, the received signal in equation (2.1) is approximated by $s(t-\tau_n) \approx s(t)$ [1]. Notice that we can separate $s(t)$ effectively from the array manipulation vector $\mathbf{v}(\theta)$, which is given by

$$\mathbf{v}(\theta) = \begin{bmatrix} e^{j2\pi d_x(0)\frac{\sin\theta}{\lambda}} \\ e^{j2\pi d_x(1)\frac{\sin\theta}{\lambda}} \\ \cdot \\ \cdot \\ \cdot \\ e^{j2\pi d_x(N-1)\frac{\sin\theta}{\lambda}} \end{bmatrix}. \tag{2.3}$$

Incorporating $d_x = \frac{\lambda}{2}$, $\mathbf{v}(\theta)$ is then simplified [2] to

$$\mathbf{v}(\theta) = \begin{bmatrix} e^{j(0)\pi\sin\theta} \\ e^{j(1)\pi\sin\theta} \\ \cdot \\ \cdot \\ \cdot \\ e^{j(N-1)\pi\sin\theta} \end{bmatrix}. \tag{2.4}$$

2.1.2 The 2-D Array Manipulation Vector

Taking the results of our simplified uniform linear array manipulation vector, $\mathbf{v}(\theta)$, we can apply this to the 2-dimensional case shown in Figure 2.2.

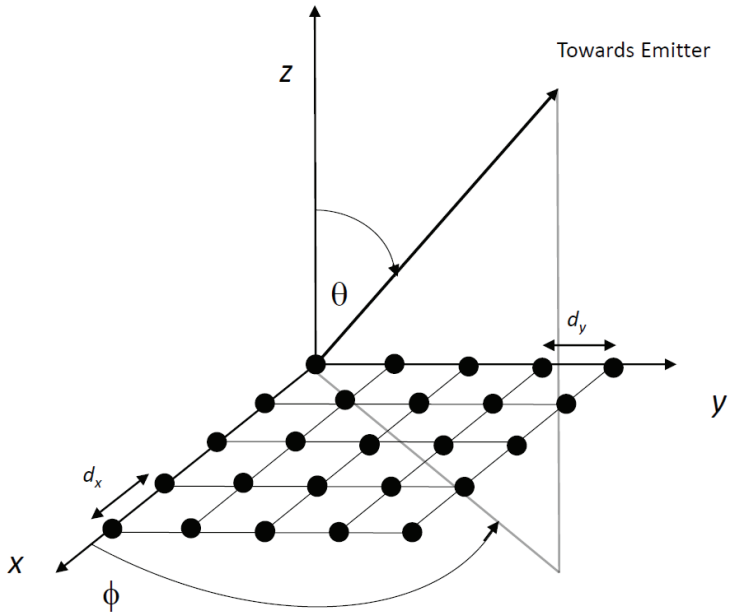

Figure 2.2. 2-d isotropic, uniform planar array with 5 elements along both the x and y axis.

In the case where $d_x = d_y = \frac{\lambda}{2}$ for our uniform, planar 2-d array, the array manipulation

matrix, $\mathbf{V}(\theta, \phi)$, becomes an $N \times M$ matrix in general [2]. In this case, N is the number of elements in the x-direction, and M is the number of elements in the y-direction. Elements along the y-axis are then identified by m: $0, 1, 2, ..., M$, where each element of the matrix $\mathbf{V}(\theta, \phi)$ is of the form

$$\exp[j\pi(n\sin\theta\cos\phi + m\sin\theta\sin\phi)]. \tag{2.5}$$

This resulting matrix, $\mathbf{V}(\theta, \phi)$, can be reshaped by stacking the vectors to obtain an $NM \times 1$ array manipulation vector $\mathbf{v}(\theta, \phi)$ for use in the 2-d case [2]. Mathematically the **vec** operation (which stands for vectorize) is used [2].

2.1.3 The 3-D Array Manipulation Vector

The concept discussed in the previous section can now be applied to 3-dimensional case as shown in Figure 2.3. In the case where $d_x = d_y = d_z = \frac{\lambda}{2}$ for our uniform 3-d volumetric array, the array manipulation matrix is a $N \times M \times L$. Elements along the z-axis are then identified by l: $0, 1, 2, ..., L$, where each element of the matrix $\mathbf{V}(\theta, \phi)$ is of the form

$$\exp[j\pi(n\sin\theta\cos\phi + m\sin\theta\sin\phi + l\cos\theta)], \tag{2.6}$$

which is based on the $x(n), y(m)$, and $z(l)$ element's position in the array and respective to the reference point (origin of zero). Like in the 2-d case, the resulting matrix, $\mathbf{V}(\theta, \phi)$, can be reshaped by stacking the vectors to obtain an $NML \times 1$ array manipulation vector $\mathbf{v}(\theta, \phi)$ for use in the 3-d case.

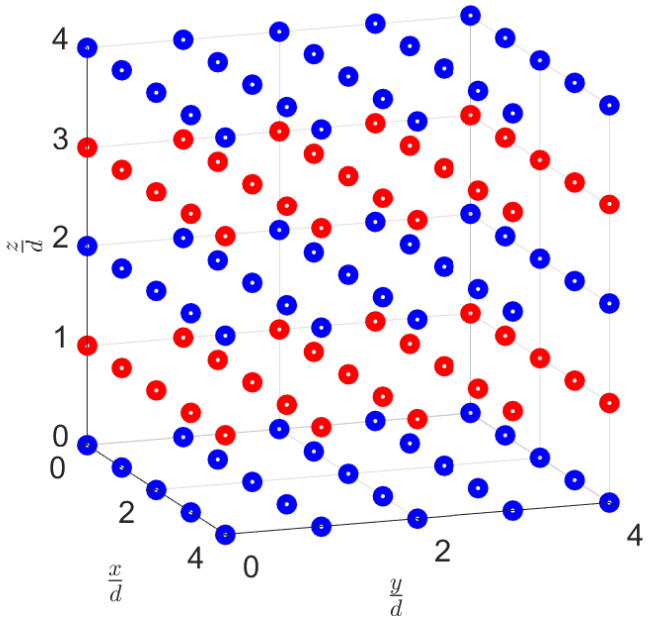

Figure 2.3. Isotropic, uniform volumetric array with 5 elements along x, y, and z axes spaced integer multiples of d apart.

2.2 Normalized Patterns of an Isotropic 3-d Uniform, Volumetric Array

It is good to get a spatial consideration of the normalized gain factors for these arrays, rather than just looking at complex-valued vectors. Consider Figure 2.3 and consider what the normalized gain pattern for this antenna array would look like for isotropic elements. It can be shown that the normalized power signal output of an antenna array is [1]

$$\mathbf{P}(\theta, \phi) = |\mathbf{v}^H(\theta, \phi)\mathbf{v}(\theta, \phi)|^2, \tag{2.7}$$

where $\mathbf{P}(\theta, \phi)$ is the unit power beamformer output and H is the Hermitian operator (or conjugate transpose).

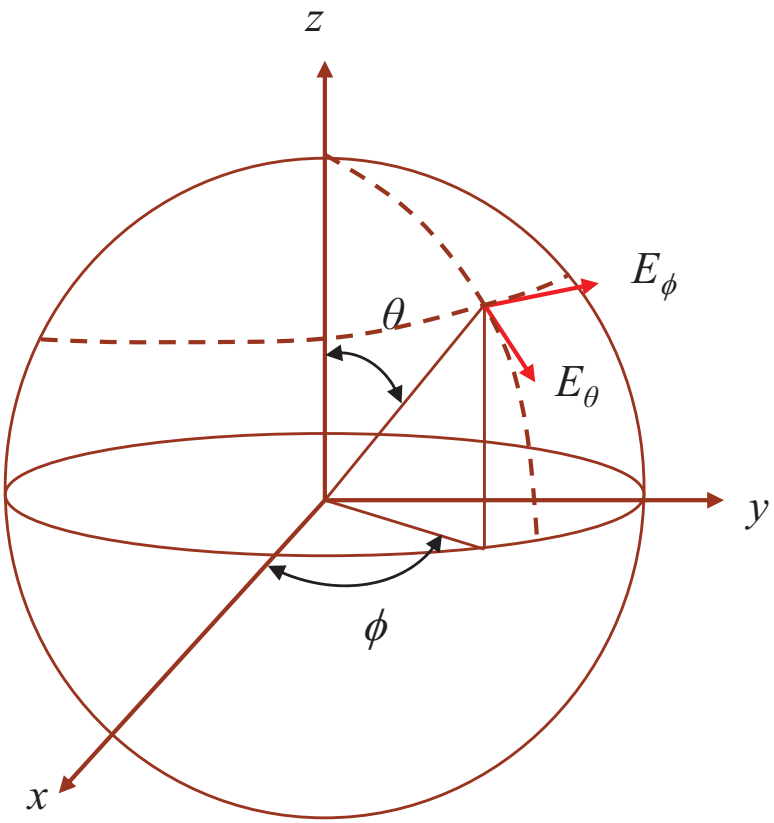

Figure 2.4. Spherical, Cartesian coordinate system with defined polarization vectors for θ and ϕ.

Also, it is important to consider the coordinate geometry of the incident plane wave and its polarization components in terms of θ and ϕ. This geometry is shown in Figure 2.4.

Looking at Figures 2.5-2.7, we can get an intuitive feel for the gain pattern of a 3-d isotropic antenna array for the model shown in Figure 2.3. The power patterns are normalized to the main beam maximum.

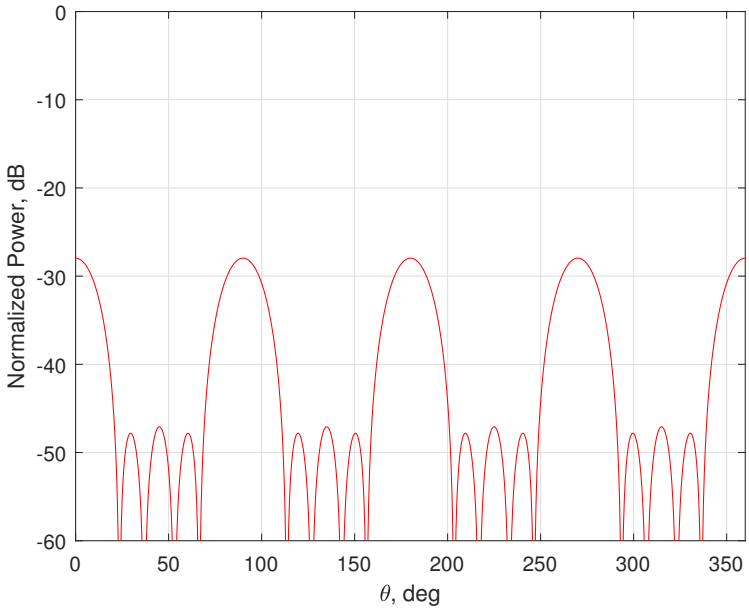

Figure 2.5. Normalized gain $\phi = 0°$ of an isotropic, 3-d uniform volumetric array with 5 elements spaced $\frac{\lambda}{2}$ along x, y, and z axes scanned to $\theta_s = \phi_s = 90°$.

Figure 2.5 shows a 2-d cut of the normalized gain pattern of a 3-d isotropic array, with $\phi = 90°$ while varying θ from 0 to 360°. The plot shows the normalized gain pattern in transmitting mode for a scanning direction of $\theta_s = \phi_s = 90°$. By reciprocity [4], this is the same pattern for the array in the receiving mode. The low levels in Figure 2.5 are due to the fact that this ϕ cut is not through the main beam for this scan angle.

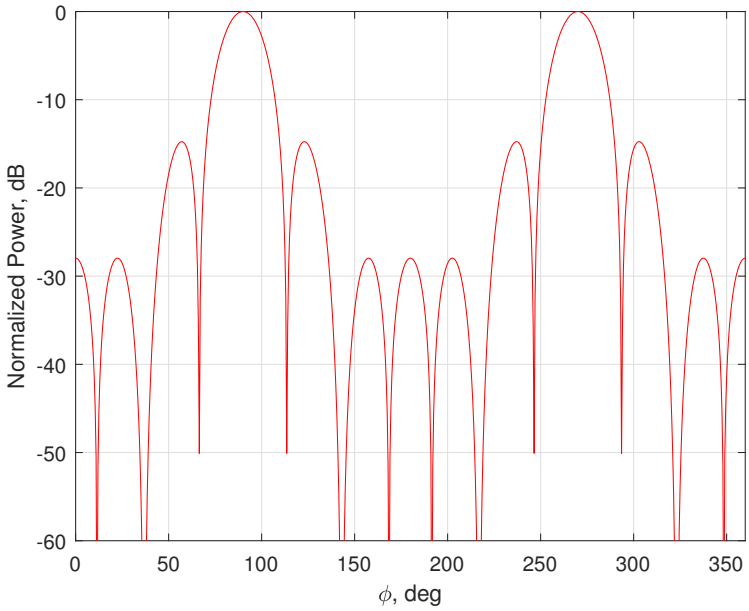

Figure 2.6. Normalized gain $\theta = 90°$ of an isotropic, 3-d uniform volumetric array with 5 elements spaced $\frac{\lambda}{2}$ along x, y, and z axes scanned to $\theta_s = \phi_s = 90°$.

Figure 2.6 shows a cut of the normalized gain pattern of a 3-d isotropic array, with $\theta = 90°$ while varying ϕ from 0 to 360°. The plot shows the normalized gain pattern in transmitting mode for a scanning direction of $\theta_s = \phi_s = 90°$. By reciprocity [4], this is the same pattern for the array in the receiving mode. The peak values at 90° and 180° are the main beams that can be seen clearly in Figure 2.7.

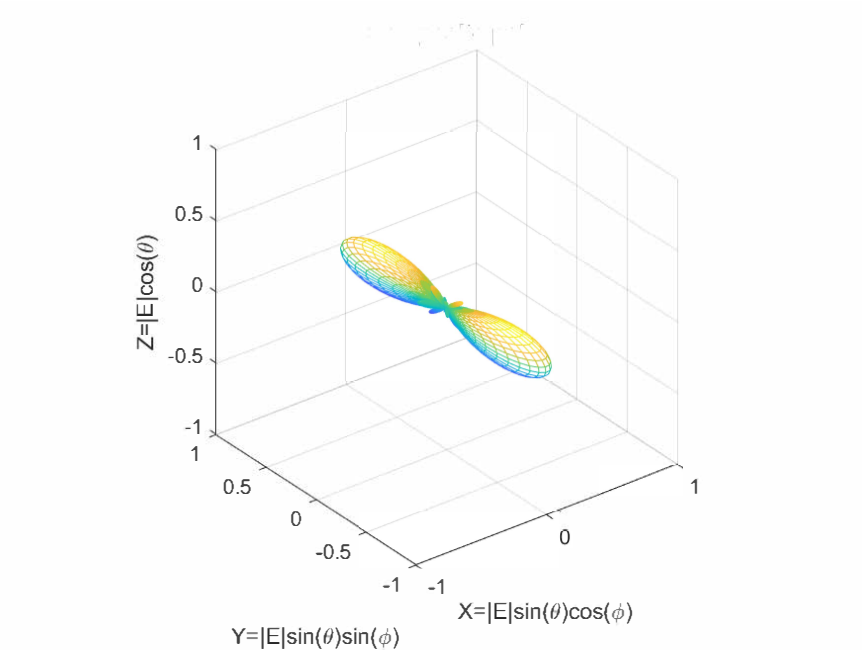

Figure 2.7. 3-d mesh plot of the gain pattern for an isotropic, 3-d uniform volumetric array with 5 elements along x, y, and z axes scanned to $\theta_s = \phi_s = 90°$.

Next, Figure 2.7 shows a 3-d mesh plot of the gain pattern we would expect of a 3-d uniform array of isotropic elements scanned to $\theta_s = \phi_s = 90°$. The two main lobes are generally undesirable, leading to reduced array gain and ambiguities in DF.

2.3 Normalized Pattern of a Colinear Dipole Array

Although mutual coupling is an important implementation concept and is tackled fully in papers such as [13], it is beyond the scope of this thesis. Neglecting mutual coupling, the normalized pattern of an antenna array is

$$\mathbf{f}(\theta, \phi) = \mathbf{E}(\theta, \phi)\mathbf{v}(\theta, \phi), \tag{2.8}$$

where $\mathbf{E}(\theta, \phi)$ is the element factor of a single antenna and $\mathbf{v}(\theta, \phi)$ is the normalized array factor [4] (which is the array manipulation factor discussed previously). In the case of a 3-d array of colinear dipoles parallel to the x, y, or z-axis shown in Figure 2.8, the element

factor $\mathbf{E}(\theta, \phi)$ can have both θ and ϕ components.

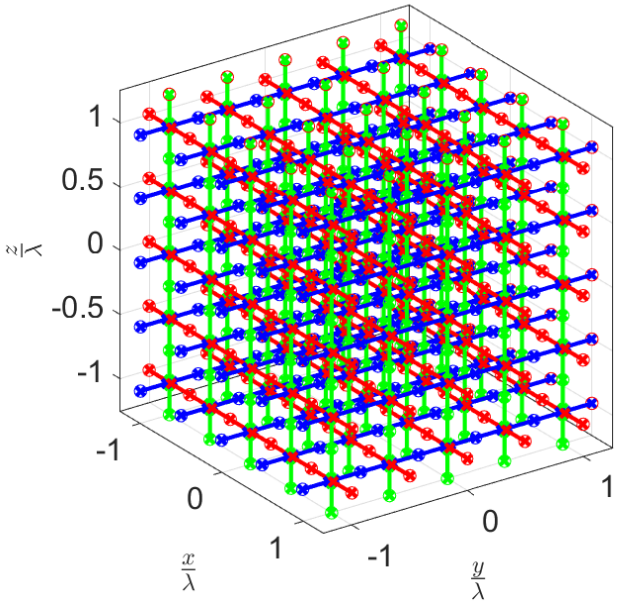

Figure 2.8. 3-d colinear dipole arrays, $N_x = N_y = N_z = 5$, where N is the number of elements per dimension spaced $\frac{\lambda}{2}$ apart, and centered at the origin.

A summary of the element factors for each dipole orientation, based on our defined coordinate system, is shown in Table 2.1 [4]. As an example, the element factor for each x, y, and z directed dipole array is shown and explored in Section 2.4. Because of each array axis-oriented alignment, the θ and ϕ components will vary.

We can now use the normalized pattern, $\mathbf{f}(\theta, \phi)$, as the array manipulation vector for the

Table 2.1. Summary of half-wave dipole element factors

Orientation	$\mathbf{E}_\theta$	$\mathbf{E}_\phi$
X Colinear	$-\frac{\cos(\frac{\pi}{2}\sin\theta\cos\phi)}{(1-\sin^2\theta\cos^2\phi)}\cos\theta\cos\phi$	$\frac{\cos(\frac{\pi}{2}\sin\theta\cos\phi)}{(1-\sin^2\theta\cos^2\phi)}\sin\phi$
Y Colinear	$-\frac{\cos(\frac{\pi}{2}\sin\theta\sin\phi)}{(1-\sin^2\theta\sin^2\phi)}\cos\theta\sin\phi$	$-\frac{\cos(\frac{\pi}{2}\sin\theta\sin\phi)}{(1-\sin^2\theta\sin^2\phi)}\cos\phi$
Z Colinear	$\frac{\cos(\frac{\pi}{2}\cos\theta)}{(1-\cos^2\theta)}\sin\theta$	0

purposes of estimating direction of arrival at the three colinear dipole arrays.

2.4 Normalized Patterns of a Half-Wave Dipole 3-d Uniform, Volumetric Array

As was shown for the 3-d isotropic array in Section 2.3, we can look at at Figure 2.7 and examine the normalized gain factors of the uniform dipole arrays. Plotting normalized patterns gives a more intuitive and spatial understanding of their normalized gain patterns, rather than the mathematical element factors listed in Table 1. Looking at Figures 2.9 and 2.10, we point to the gain patterns of a 3-d half-wave dipole, uniform volume array, with elements colinear with the x, y, and z-axes as shown.

Figure 2.9 shows 2-d cuts of the normalized gain patterns for a uniform 3-d half-wave dipole, x, y, and z-axis colinear volumetric array, with $\phi = 0°$ while varying θ from 0 to 180° for a scanning direction of $\theta_s = 90°$, $\phi_s = 0°$.

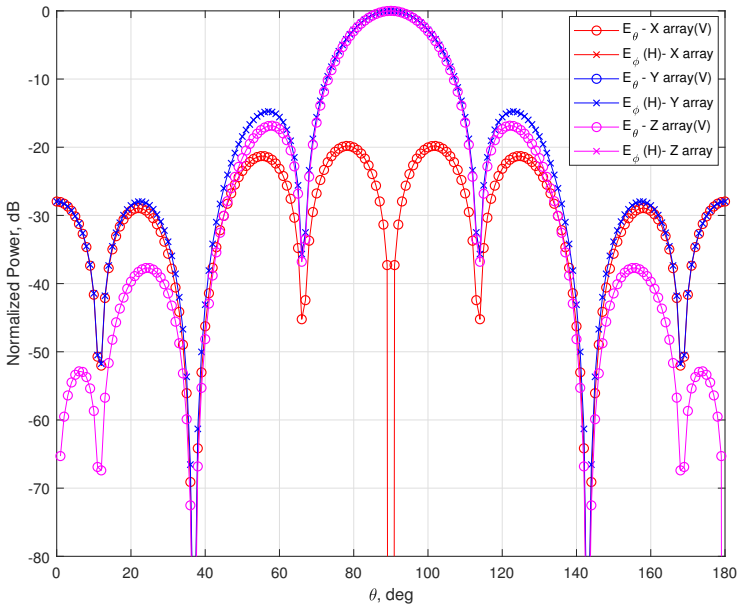

Figure 2.9. Normalized gain ($\phi = 0°$) patterns for a uniform 3-d half-wave dipole, x, y, and z-axis colinear volumetric arrays with 5 elements along x, y, and z axes and a scanning direction of $\theta_s = 90°$, $\phi_s = 0°$.

In comparison, Figure 2.10 shows 2-d cuts of the normalized gain patterns for a uniform 3-d half-wave dipole, x, y, and z-axis colinear volumetric array, with $\theta = 90°$ while varying ϕ from 0 to 360° for a scanning direction of $\theta_s = 90°$, $\phi_s = 0°$. A similar pattern results for both Figure 2.9 and 2.10 if the scan direction was set to $\theta_s = \phi_s = 90°$, however, the beam is rotated 90° around the z-axis.

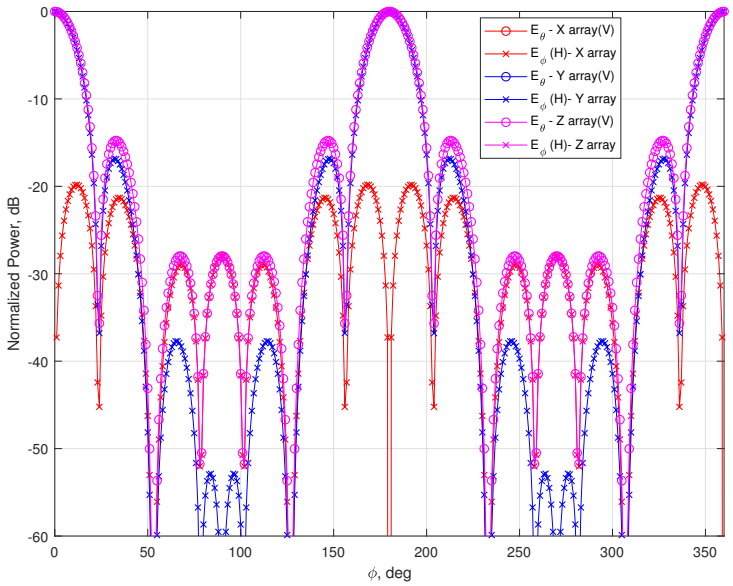

Figure 2.10. Normalized gain ($\theta = 90°$) patterns for a uniform 3-d half-wave dipole, x, y, and z-axis colinear volumetric arrays with 5 elements along x, y, and z axes and a scanning direction of $\theta_s = 90°$, $\phi_s = 0°$.

Figure 2.11 shows a 3-d mesh plot of the same z-colinear array, with a θ (vertically) polarized wave that gives a spatial feel for the gain pattern we would expect of this antenna array.

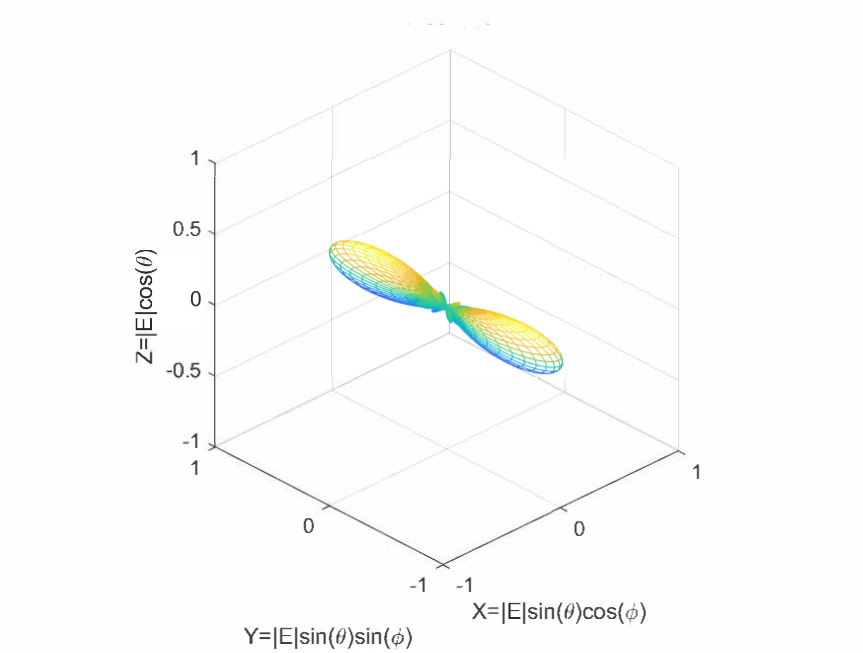

Figure 2.11. 3-d Mesh plot of the gain pattern for a vertically polarized wave for a z-colinear, half-wave dipole, 3-d uniform volumetric array with 5 elements along x, y, and z axes scanned to $\theta_s = \phi_s = 90°$.

In the case of Figure 2.11, the pattern is very similar to the isotropic pattern, because the beam is scanned broadside to the z-directed dipoles.

THIS PAGE INTENTIONALLY LEFT BLANK

CHAPTER 3:
Development of Direction Finding Estimation Techniques

3.1 Simulation Model

The estimation techniques examined in this thesis are the MLE and the MVDR [9]. It should be said in general that MLE is expected to perform better than MVDR, but at the cost of being much more computationally expensive [2]. We will compare the performance of these two estimation techniques against the CRB.

For the purposes of our estimation, we let $\mathbf{x}(t)$ be our signal plus noise model, with the assumption that the noise is temporally and spatially white complex Gaussian. To be clear, $\mathbf{x}(t)$ is a vector since $\mathbf{v}(\theta, \phi)$ is a vector. Therefore,

$$\mathbf{x}(t) = s(t)\mathbf{v}(\theta, \phi) + \mathbf{w}(t). \tag{3.1}$$

It is usual to model the amplitude of our signal, $s(t)$, to be complex Gaussian and thus it can be shown that the covariance [1] of our signal component is

$$\mathbf{C_s} = E[|s(t)|^2]\mathbf{v}(\theta, \phi)\mathbf{v}^H(\theta, \phi) = P_s\mathbf{v}(\theta, \phi)\mathbf{v}^H(\theta, \phi) \tag{3.2}$$

where E is the expectation operator, P_s is average signal power, and H is the Hermitian operator (or conjugate transpose). Since the noise is independent from the signal, the overall received signal is described by a single covariance matrix,

$$\mathbf{C_x} = \mathbf{C_s} + \sigma^2\mathbf{I}. \tag{3.3}$$

For the purposes of calculating the CRB, the Fisher information matrix, $\mathbf{F}$, can be shown to be [1]

$$\mathbf{F} = 2SNR^2(\mathbf{v}^H(\theta, \phi)\mathbf{C_x}^{-1}\mathbf{v}(\theta, \phi))(\dot{\mathbf{v}}^H(\theta, \phi)\mathbf{C_x}^{-1}\dot{\mathbf{v}}(\theta, \phi)) \tag{3.4}$$

where $\dot{\mathbf{v}}(\theta, \phi)$, is the derivative of our derived, normalized array manipulation vector with

respect to ϕ or θ, as appropriate for the parameter being estimated. Then, the CRB can be calculated as

$$\mathbf{CRB} = \frac{1}{K}\mathbf{F}^{-1}, \tag{3.5}$$

where K is the number of snapshots or independent measurements taken [1].

We now use this calculated CRB as a baseline to evaluate the effectiveness of our DOA MLE technique. First, the MLE is calculated by [2]

$$L(\theta, \phi) = -[ln(det(\mathbf{C_x})) + tr[\mathbf{C_x^{-1}}\mathbf{C_{\tilde{x}}}]], \tag{3.6}$$

where det is the determinant of our matrix, ln is the natural logarithm, and tr is the trace operator of our resultant matrix. Additionally, $\mathbf{C_{\tilde{x}}}$ is the sample correlation matrix defined by [2]

$$\mathbf{C_{\tilde{x}}} = \frac{1}{K}\sum_{k=1}^{K}\mathbf{x}_k\mathbf{x}_k^{\mathrm{H}} \tag{3.7}$$

and $\mathbf{x}_k$ is a $NML \times 1$ (for the 3-d array case) received signal which is generally a complex Gaussian random vector [2]. Once $L(\theta, \phi)$ is calculated, we find the minimum which is associated with a numbered bin of our search grid for either θ or ϕ. The estimated direction of arrival is the angle associated with the bin number with the minimum of $L(\theta, \phi)$ function.

For the MVDR estimate, we calculate the following [2]

$$\hat{Q}_{mvdr} = \mathbf{v}^H(\theta, \phi)\mathbf{C}_{\tilde{\mathbf{x}}}^{-\mathbf{1}}\mathbf{v}(\theta, \phi). \tag{3.8}$$

Moreover, like the MLE discussed previously, we find the local minimum of the function and the estimated direction of arrival are the angles associated with the closest search bin value associated with that minimum.

CHAPTER 4:
Isotropic Array Results and Analysis

4.1 MLE Performance, Experiment 1.a

For our first experiment, we look at the results of the 3-d 125 antenna array ($5 \times 5 \times 5$), 2-d 25 antenna array (5×5), and 1-d antenna array (5×1). All three arrays are isotropic, uniform antenna arrays. The number of snapshots, K, is 50 and the number of Monte-Carlo simulations is 3000. The angles of the plane wave are $\theta = 45°$ and $\phi = 30°$, respectively with 61 search bins from a scan of 30° on either side of the angle respectively. That is, the search scan of 60° for the angle of arrival is divided into 61 equally spaced angles, for a scan resolution of about 1°. The first results to be examined are the MLE variance and mean estimates for both θ and ϕ. The performance curves are shown in Figures 4.1-4.4.

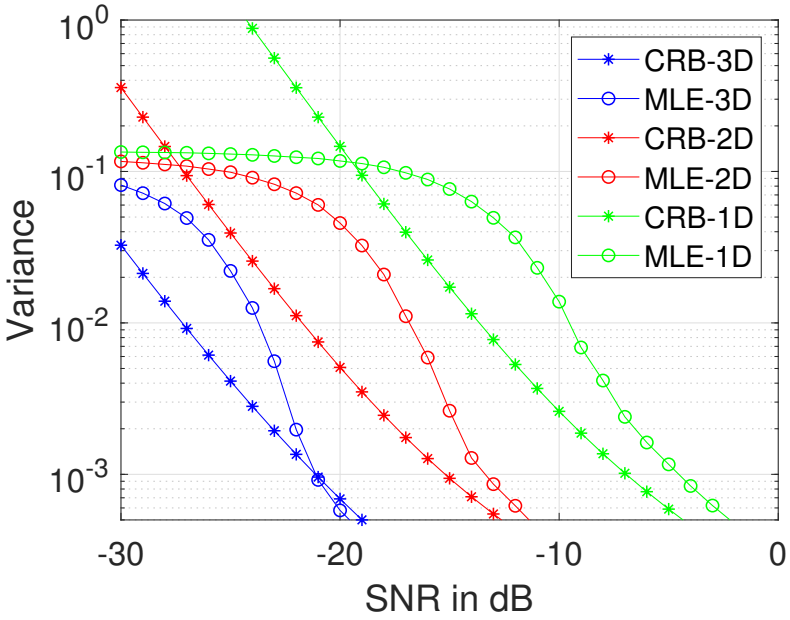

Figure 4.1. Variance for estimation of θ from the 3 isotropic, uniform arrays, 3-d cube ($5 \times 5 \times 5$) vs. 2-d square (5×5) vs. 1-d line (5×1)

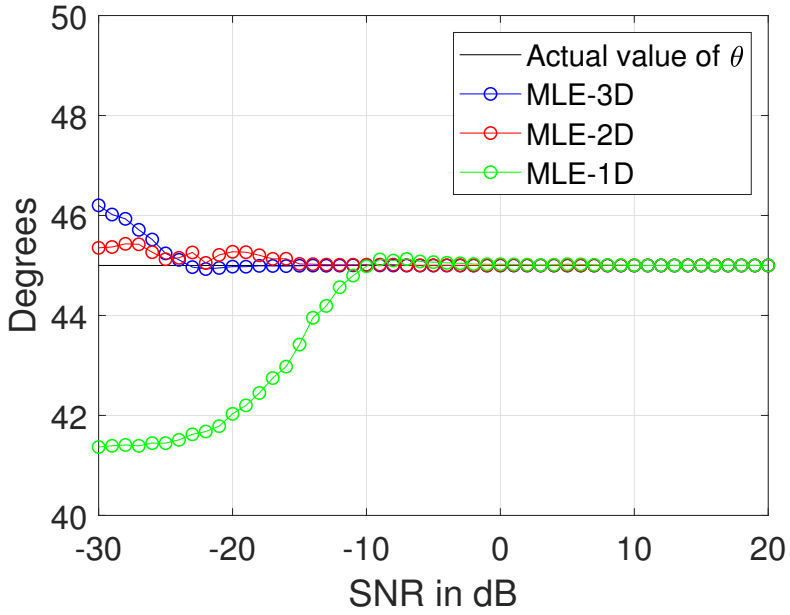

Figure 4.2. Mean for estimation of θ from the 3 isotropic, uniform arrays, 3-d cube $(5 \times 5 \times 5)$ vs. 2-d square (5×5) vs. 1-d line (5×1)

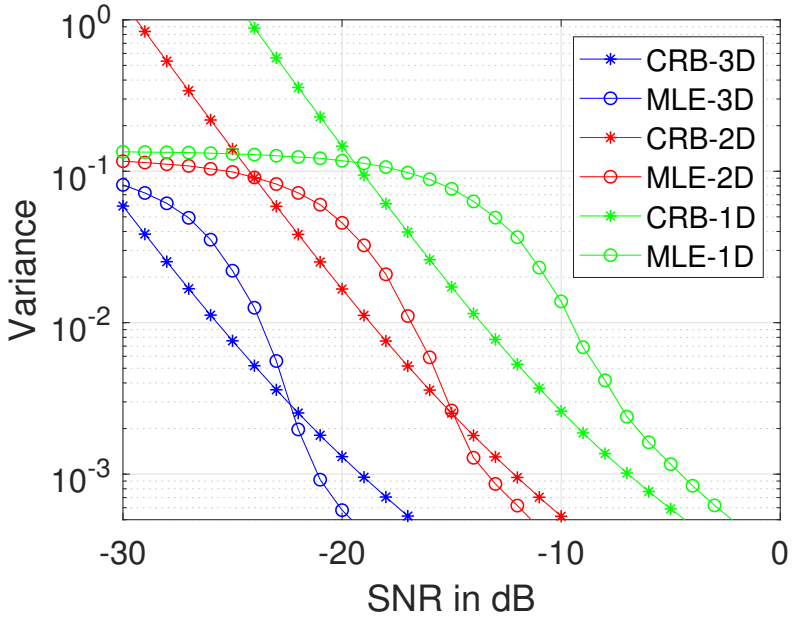

Figure 4.3. Variance for estimation of ϕ from the 3 isotropic, uniform arrays, 3-d cube $(5 \times 5 \times 5)$ vs. 2-d square (5×5) vs. 1-d line (5×1)

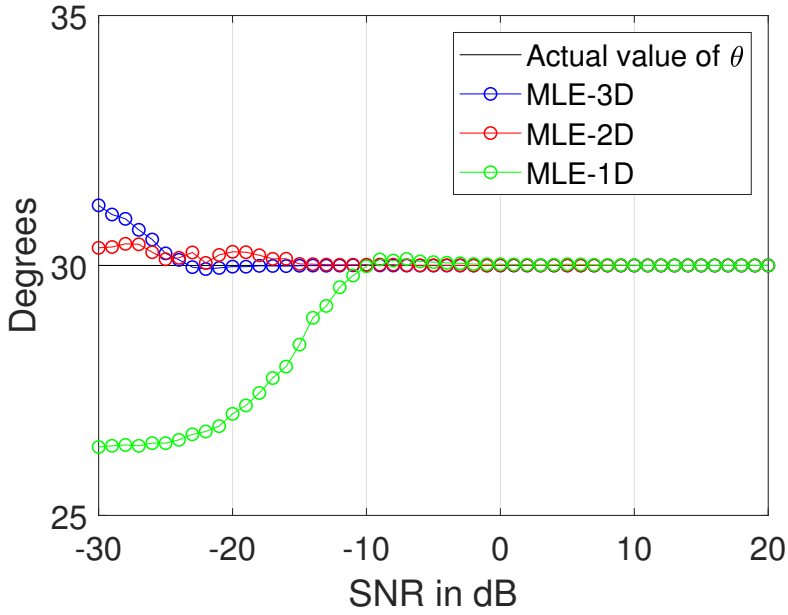

Figure 4.4. Mean for estimation of ϕ from the 3 isotropic, uniform arrays, 3-d cube $(5 \times 5 \times 5)$ vs. 2-d square (5×5) vs. 1-d line (5×1)

Examining the variance of the estimates in Figures 4.1 and 4.3, it is seen that the MLE performs extremely well, closely following the CRB for each respective dimensional array. Next, the mean estimates shown in Figures 4.2 and 4.3 are accurate with respect to the actual angle of arrival of the impinging signal. This accuracy is due to choosing favorable (broadside) angles with respect to the orientation of the 1-d array. That is, we assume a 1-d array along the z-axis for the θ estimate, and we assume a 1-d array along the x-axis for the ϕ estimate. Moreover, note that the mean angle estimate of 3-d converges to true angle first followed by the angle estimate of 2-d, with the angle estimate of the 1-d array converging to true angle last. The increase in performance makes sense considering the increase in array size: 5 antennas for 1-d (5×1), 25 antennas for 2-d (5×5), and 125 antennas for 3-d $(5 \times 5 \times 5)$. The variances of these arrays are largest when the mean estimates are inaccurate, i.e. when the SNR is lowest. This low variance (for all three arrays) is about 0.1 at -30 dB SNR (which is expected since this SNR is obviously very low). To make a proper comparison, we compare performance when all the mean estimates become accurate. The last array to become accurate is the 1-d array which is at -10 dB SNR. Inspecting Figure 4.3 at the variance of 10^{-2}, we notice that the curves are separated by a performance

improvement of about 7 dB from 1-d to 2-d and about the same improvement from 2-d to 3-d. To summarize, the performance of the 3-d array is superior compared to 2-d, and 2-d's performance is superior to 1-d.

4.2 MVDR Performance, Experiment 1.b

As mentioned earlier, MVDR is another technique we implement in this thesis. MVDR is potentially more efficient than MLE but it comes with its own computational issues. For this experiment, we modify slightly the parameters of our earlier experiment due to some of the limitations of the MVDR estimation technique. For large sparse and ill-conditioned matrices, the inverse operation of the spatial sampling matrix required by equation (3.8) can yield ill-defined results when evaluated numerically. There are numerous papers that mention the ill-defined matrix inverse problem, and some that have solutions to help deal with the issue [14]. However, for our simulation we'll reduce the number of antennas in any given array to three in any (x, y, or z-axis) direction. That is, three antennas for 1-d (3×1), 9 antennas for 2-d (3×3), and 27 antennas for 3-d ($3 \times 3 \times 3$). This is essentially utilizing the exact array shown in Figure 1.1 of the Introduction section. The number of snapshots, K, is still 50 and the number of Monte-Carlo simulations is still 3000. In addition, the angles of the plane wave are still $\theta = 45°$ and $\phi = 30°$, respectively with 61 search bins from a scan of 30° on either side of the two given angles. The performance results are shown in Figures 4.5-4.8.

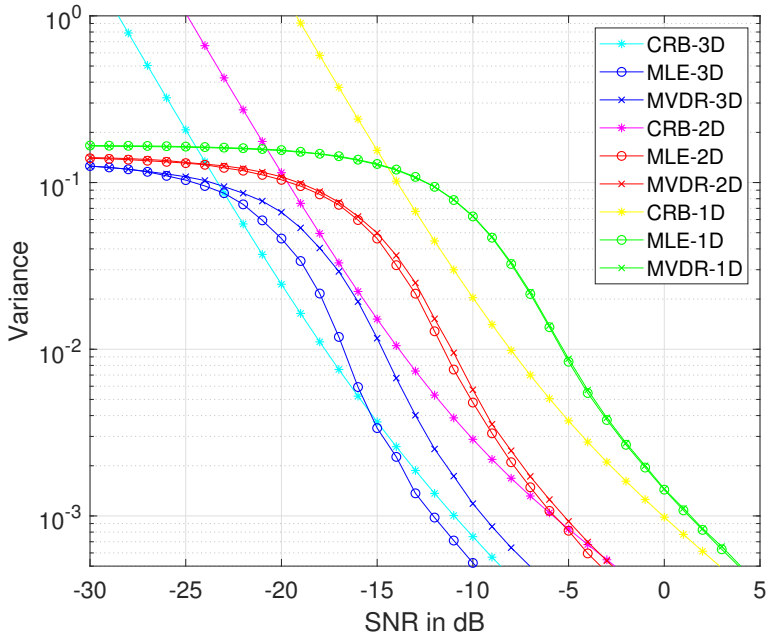

Figure 4.5. Variance for estimation of θ from the 3 isotropic, uniform arrays, 3-d cube $(3 \times 3 \times 3)$ vs. 2-d square (3×3) vs. 1-d line (3×1)

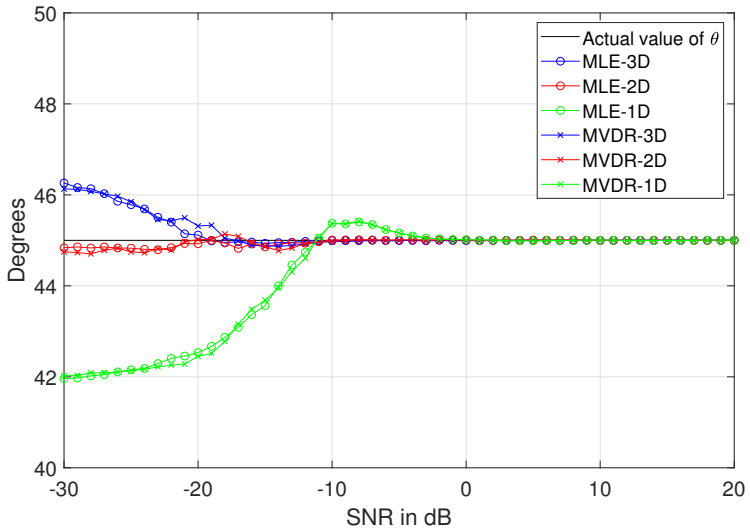

Figure 4.6. Mean for estimation of θ from the 3 isotropic, uniform arrays, 3-d cube $(3 \times 3 \times 3)$ vs. 2-d square (3×3) vs. 1-d line (3×1)

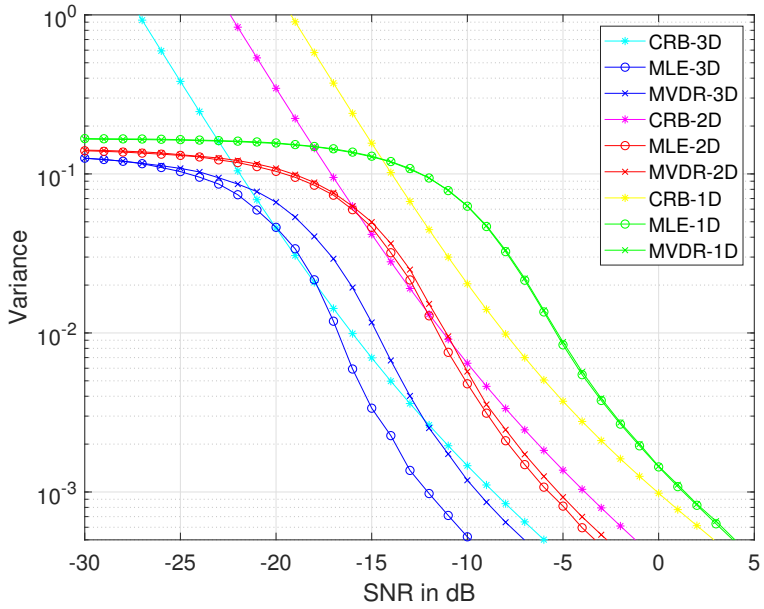

Figure 4.7. Variance for estimation of ϕ from the 3 isotropic, uniform arrays, 3-d cube $(3 \times 3 \times 3)$ vs. 2-d square (3×3) vs. 1-d line (3×1)

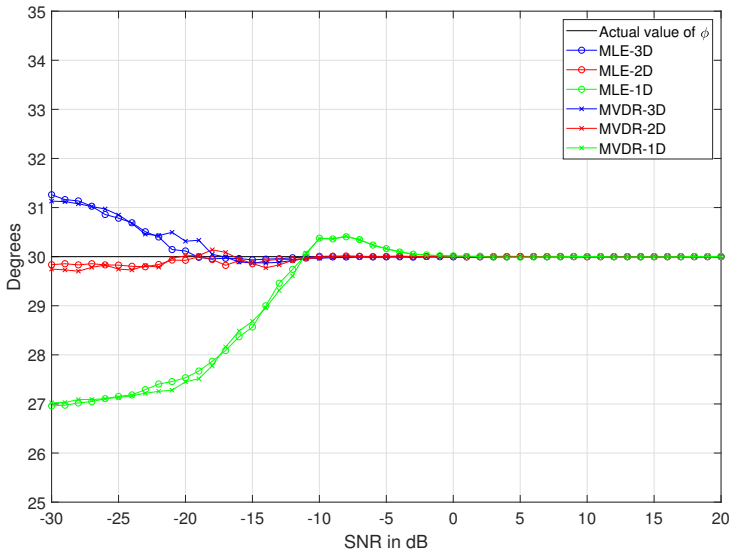

Figure 4.8. Mean for estimation of ϕ from the 3 isotropic, uniform arrays, 3-d cube $(3 \times 3 \times 3)$ vs. 2-d square (3×3) vs. 1-d line (3×1)

Now examining the variance of the estimates in Figure 4.5 and 4.7, we observe that MVDR performs nearly as well as the MLE, closely following the respective CRB curves for each array. Although the MVDR does lag the MLE estimate slightly (shown in Figures 4.6 and 4.8), there is a reason it performs well in this experiment. We assume a favorable geometry for the angles being estimated. That is, for the θ estimate we assume a 1-d array along the z-axis, and for the ϕ estimate we assume a 1-d array along the x-axis. This is because a 1-d array along the z-axis would be completely independent of a ϕ angle of estimation. Second, there is sufficient snapshots, K, such that the MVDR performs nearly identical to MLE due to isotropic modeling. Our next experiment is modified slightly to show the impact of reducing K. Finally, similar to the MLE estimates shown previously, the increase in performance makes sense considering the increase in array size: three antennas for 1-d (3×1), nine antennas for 2-d (3×3), and 27 antennas for 3-d ($3 \times 3 \times 3$).

4.3 MLE vs. MVDR Performance, Experiment 1.c

For our final isotropic experiment, we reduce K down to 35. This is to highlight the performance degradation of the MVDR estimation technique when compared to MLE if there is insufficient snapshots collected. To summarize, K is reduced to 35 and the number of Monte-Carlo simulations is still 3000. In addition, the angles of the plane wave are still $\theta = 45°$ and $\phi = 30°$, respectively with 61 search bins from a scan of 30° on either side of the angle. The performance results are shown in Figures 4.9-4.12.

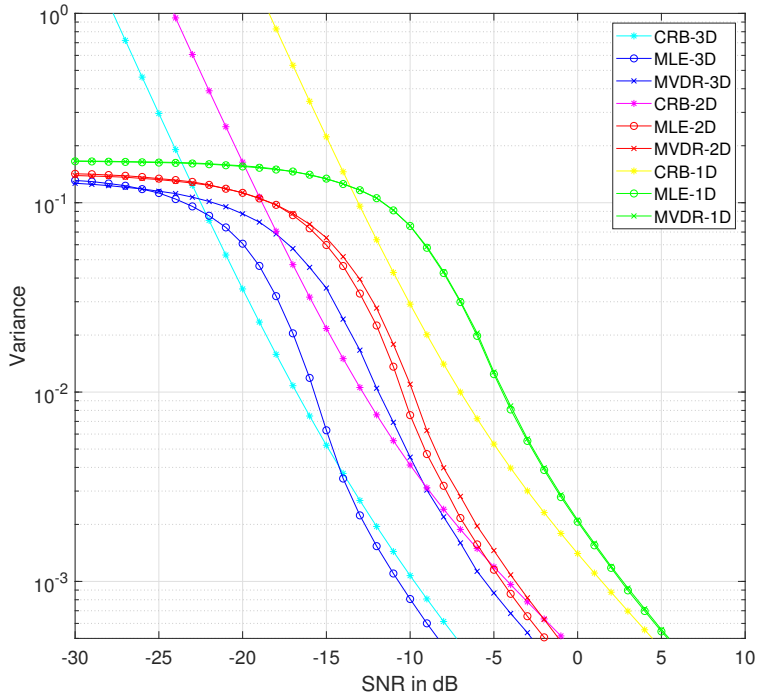

Figure 4.9. Variance for estimation of θ from the 3 isotropic, uniform arrays, 3-d cube $(3 \times 3 \times 3)$ vs. 2-d square (3×3) vs. 1-d line (3×1)

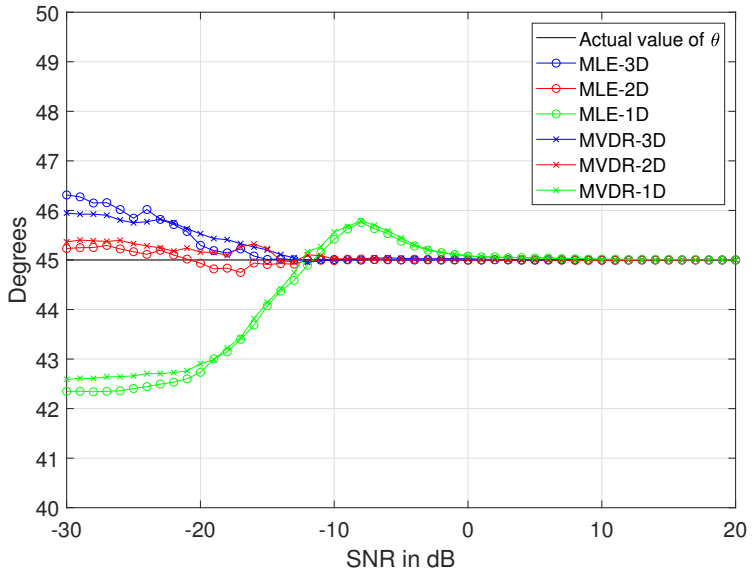

Figure 4.10. Mean for estimation of θ from the 3 isotropic, uniform arrays, 3-d cube $(3 \times 3 \times 3)$ vs. 2-d square (3×3) vs. 1-d line (3×1)

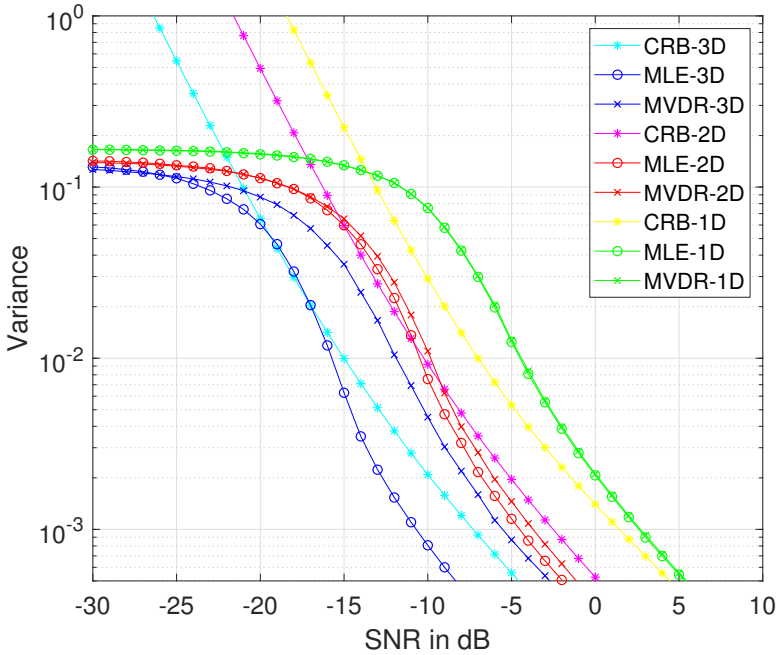

Figure 4.11. Variance for estimation of ϕ from the 3 isotropic, uniform arrays, 3-d cube $(3 \times 3 \times 3)$ vs. 2-d square (3×3) vs. 1-d line (3×1)

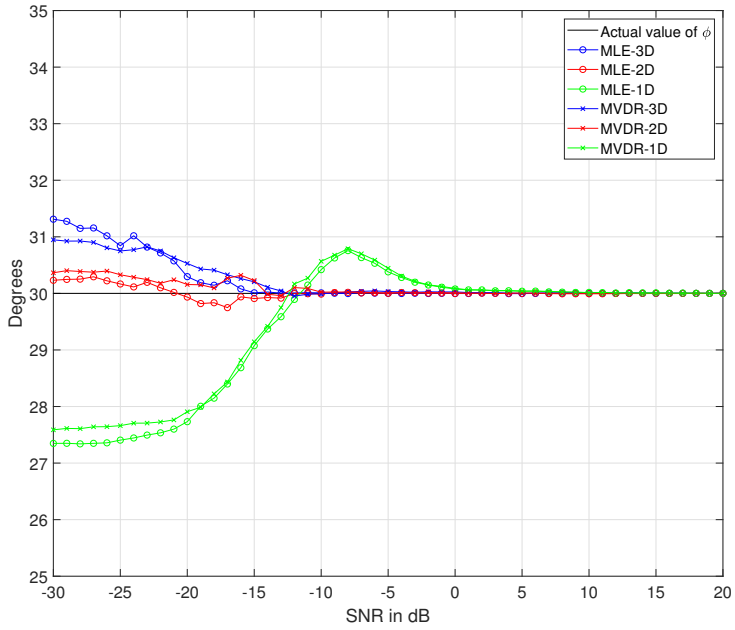

Figure 4.12. Mean for estimation of ϕ from the 3 isotropic, uniform arrays, 3-d cube $(3 \times 3 \times 3)$ vs. 2-d square (3×3) vs. 1-d line (3×1)

Examining the variance of each array and corresponding technique in Figure 4.9 and 4.11, it is clear that the MVDR lags behind the performance of the MLE, due to the reduction of K from 50 to 35. The change in K is especially notable for the 3-d array compared to 2-d and 1-d. The mean estimates of this experiment reflect slightly reduced MVDR variance performance when compared to MLE for each respective array, as shown in Figures 4.10 and 4.12. It is important to note that although the MVDR may produce a mean estimate closer to the true AOA at extremely low SNRs, it is a less reliable mean estimate than MLE. The lesser performance of MVDR compared to MLE is shown in the gap in variance of the two estimators in Figures 4.9 and 4.11, most notably for the 3-d MVDR performance compared to MLE. To summarize, by reducing the number of snapshots to 35 as opposed to 50 from Experiment 1.b in Section 4.2, it can be observed that the MLE performs better than MVDR specially in the case of 3-d antenna volumetric array.

4.4 Summary of Isotropic Results and Findings

In this section, our experiments showed the numerical benefit of increasing the number of elements and dimension of an antenna array using isotropic antenna elements. Additionally, it showed the accuracy, reliability, and some limitations of both the MLE and MVDR estimation techniques. In the next section, we will expand our model by considering practical antenna elements and the polarization of the incident wave impinging upon the array.

THIS PAGE INTENTIONALLY LEFT BLANK

CHAPTER 5:
3-d Dipole Array Results and Analysis

Now that we have seen the motivation for implementing a 3-d array, we further expand our 3-d model to include half-wave dipole antenna elements (such as in Figure 2.4) and include the polarization of the incident wave. For our experiments, we assume the incident wave to be θ polarized (refer to Table 1). We first repeat previous experiments under these conditions by first performing MLE results and we then compare to the MVDR estimation technique.

5.1 MLE Performance, Experiment 2

For our next experiment, we replace our isotropic antenna elements with half-wave dipole antennas (as shown in Figure 2.4) and assume the incident wave to be θ polarized (refer to Table 1). We compare the results from three 3-d ($3 \times 3 \times 3$) arrays of colinear dipoles (x, y, and z, respectively). For these remaining experiments, we reduce the number of antennas such that any array configuration has three elements per dimension. That is, three antennas for 1-d (3×1), nine antennas for 2-d (3×3), and 27 antennas for 3-d ($3 \times 3 \times 3$), as shown in Figure 1.2. Similar to our first isotropic antenna simulations, K is 50 and the number of Monte-Carlo simulations is 3000. The angles of the plane wave are 45° and 30°, respectively with 61 search bins from a scan of 30° on either side of the two given angles. Again, the search scan of 60° for the angle of arrival is divided into 61 equally spaced angles, for a scan resolution of about 1° . The performance of the estimators are shown in Figures 5.1-5.4.

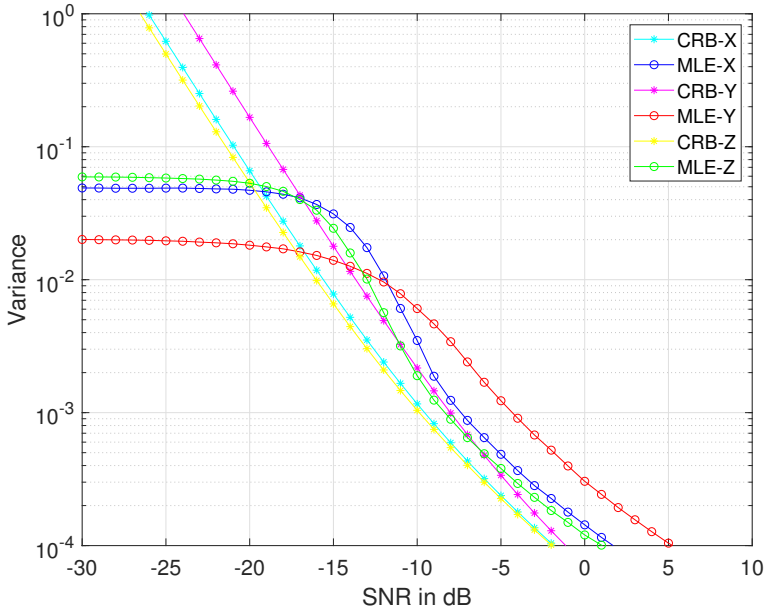

Figure 5.1. Variance for estimation of θ from the 3-d colinear, dipole arrays

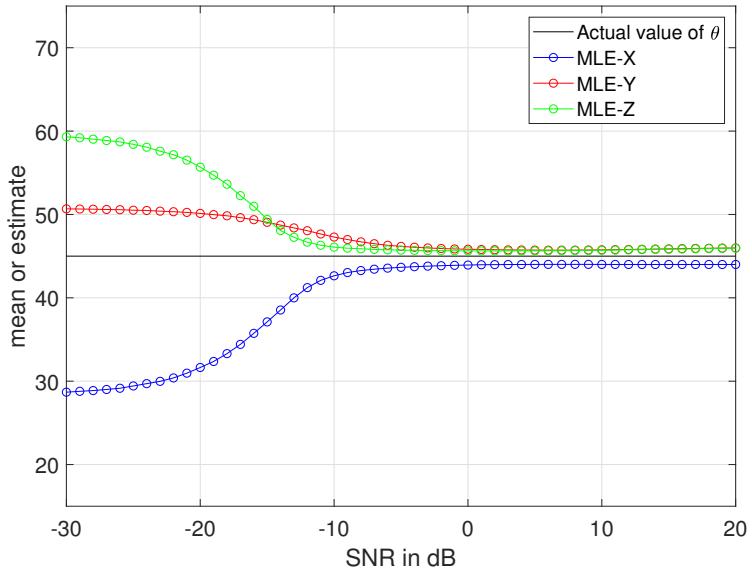

Figure 5.2. Mean estimates of θ from the 3-d colinear, dipole arrays

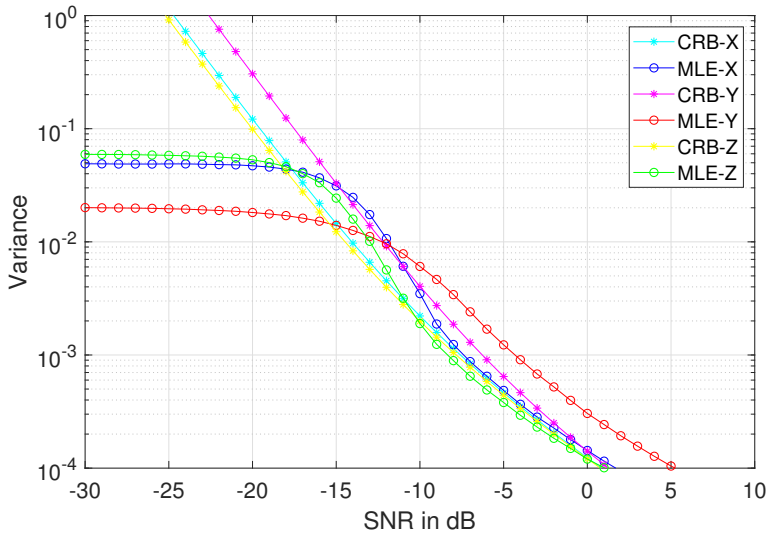

Figure 5.3. Variance for estimation of ϕ from the 3-d colinear, dipole Arrays

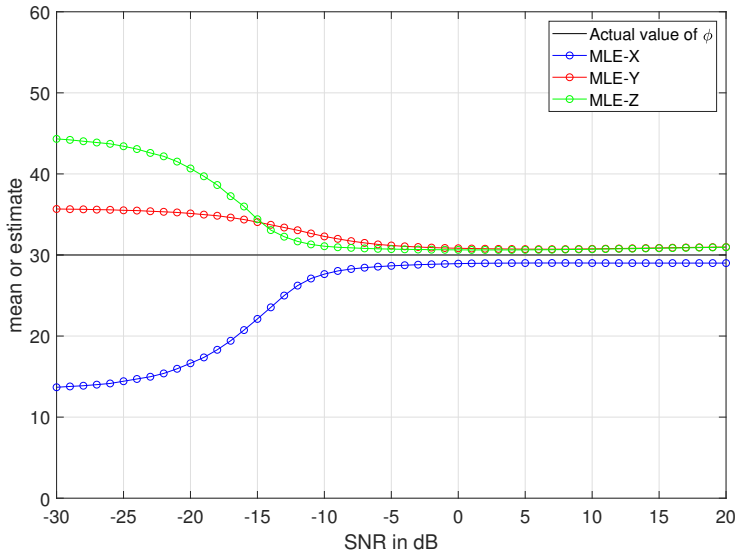

Figure 5.4. Mean estimates of ϕ from the 3-d colinear, dipole arrays

Examining the variances in Figures 5.1 and 5.3, it can be seen that the performance separation of MLE to CRB for each respective array is in the order we expect (due to element factors listed in Table 1), with the z-axis array performing the best, and y-axis array performing the

worst. The variance of x, y, and z estimates improves past 10^{-1}, but they are separated by a performance improvement of about 1 dB from z to x arrays, and about 4 dB from x to y arrays. This performance in the variance closely reflects the separation of our CRB for each respective array (albeit smaller gaps).

The mean estimates shown in Figures 5.2 and 5.4 correspond to the variance performance shown in Figures 5.1 and 5.3. For example, mean angle estimate for the y-axis converges to the true angle last in Figures 5.2 and 5.4 and as such its variance is farthest from its corresponding CRB.

For our next experiments, we consider new incident plane wave angles and examine the resulting estimates of the MLE technique with 3-d colinear dipole arrays.

5.2 MLE Performance, Experiment 3

For the last experiment, we still assume the incident wave to be θ polarized (refer to Table 1), and we compare the results from three different ($3\times3\times3$) arrays of colinear dipoles (x, y, and z, respectively). The number of snapshots has been increased to 65 and the number of Monte-Carlo simulations is still 3000. The angles of the plane wave are 75° and 105°, with 61 search bins from a scan of 30° on either side of the θ and ϕ true angle respectively. Again, the search scan of 60° for the angle of arrival is divided into 61 equally spaced angles, for a scan resolution of about 1° . The performance results are shown in Figures 5.5-5.8.

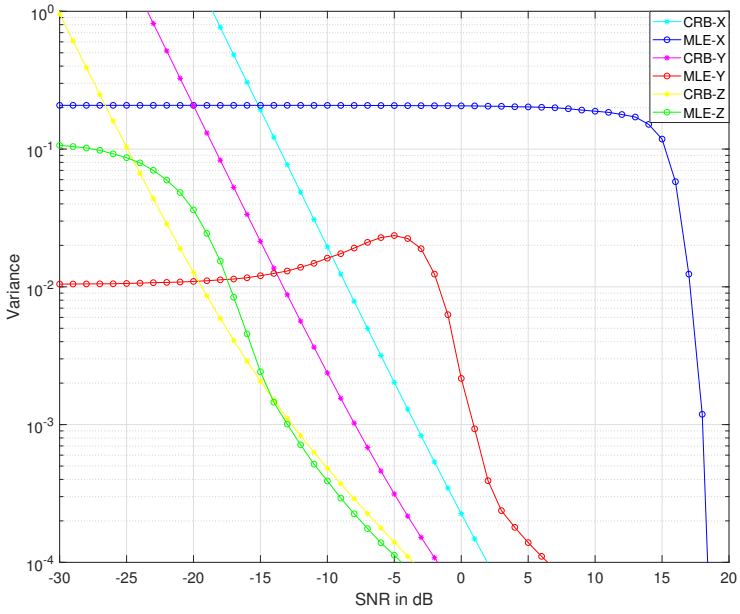

Figure 5.5. Variance for estimation of θ from the 3-d colinear, dipole arrays

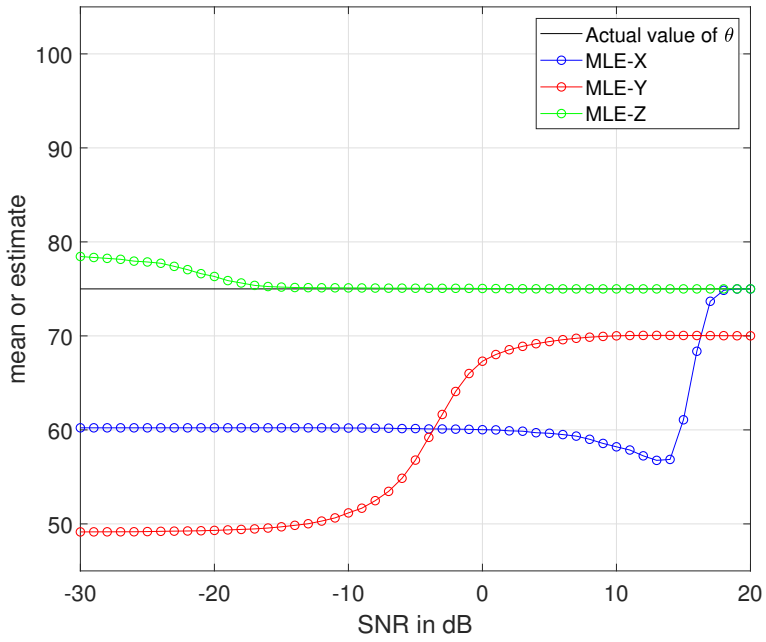

Figure 5.6. Mean estimates of θ from the 3-d colinear, dipole arrays

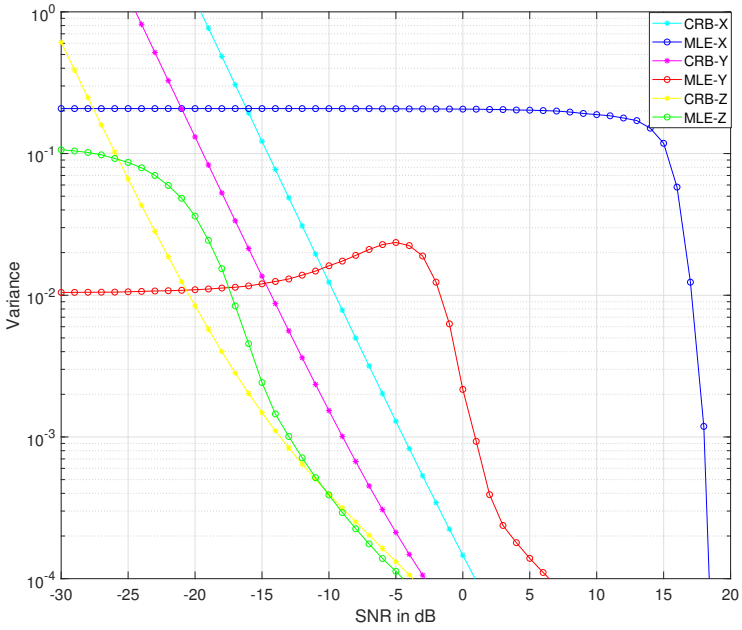

Figure 5.7. Variance for estimation of ϕ from the 3-d colinear, dipole arrays

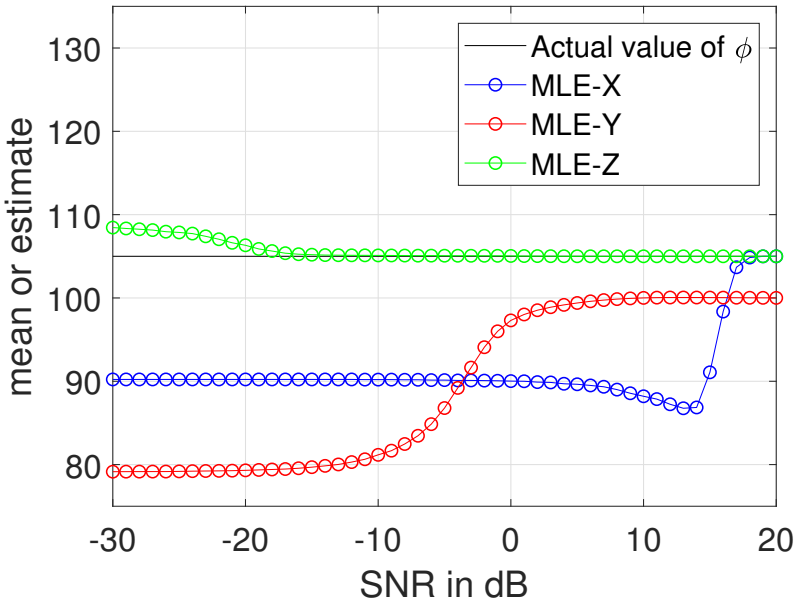

Figure 5.8. Mean estimates of ϕ from the 3-d colinear, dipole arrays

This experiment shows the significant effect of the polarization of the incident wave and the orientation of each colinear dipole axis with respect to the performance of the estimators. Most notably, this impact on performance due to polarization is true for the x-axis colinear dipole array. Looking at Figures 5.5 and 5.7, we can see that the variance of the x-axis colinear dipole array is nearly 15 dB (delta) from its theoretical CRB. The gap in performance correlates with the fact that the mean estimate does not converge to the true angle until a very large SNR of 17 dB SNR in Figures 5.6 and 5.8. Additionally, the variance of the y-axis array lags its respective CRB by around 5 dB, which is a direct result from it's unfavorable position for this AOA. Of note, it would appear that the y-axis array converges to a lower variance than the x-axis array, which seems to suggest better performance (which we know not to be true). This issue is explained when the mean estimates are examined in the next paragraph. The z-axis array continues to perform best due to its favorable polarization and orientation with the incident wave, with its variance closely following it's respective CRB as expected.

Looking at Figures 5.6 and 5.8 for the mean estimates of θ and ϕ respectively, we see that the x-axis array requires a high SNR of 17 dB. Anticipating the need for a higher K, we increase the number of snapshots to 65 for this particular experiment. The y-axis produces mean estimates at lower SNR than the x-axis. But these estimates do not converge to the true angles (both being off by around 5°). Of course, the consistent estimates would produce lower variance as noted in previous paragraph but we note that the angle estimate themselves are incorrect. However, the z-axis array produces a precise mean estimate down to -20 dB SNR and only varies 4° all the way down to -30 dB SNR.

5.3 Summary of 3-d Dipole Results and Findings

In this section, our experiments showed the effect of both polarization and geometric orientation of the real dipole elements with respect to the incident plane wave impinging on the antenna array. Additionally, it showed some limitations of the MLE, and particularly MVDR estimation technique, when considering real antenna elements and polarized waves. We conclude that the polarization and normalized gain patterns (see Figure 2.8) provided intuition for the performance of a respective colinear dipole array based on the angle of incidence for a plane wave and its polarization, which were confirmed by our estimation performance and results.

These findings are important to understand the benefit of having 3 orthogonal arrays in terms of estimation of any incident wave AOA. Having 3 separate orthogonal arrays ensures that at least one array has a favorable orientation and polarization, such as was shown in Experiment 3.

CHAPTER 6:
Conclusion

6.1 Summary and Conclusion

In this thesis, we examined the problem of direction of arrival estimation using a 1-d, 2-d, and 3-d uniform isotropic antenna arrays. We compared the DF effectiveness of a 1-d, 2-d, and 3-d isotropic uniform arrays to evaluate the advantages and performance of each configuration. We then compared the results obtained from an isotropic 3-d array with those obtained by using half-wave dipole antenna elements. We evaluated the performance using the MLE technique over varying angles of incidence as a function of SNR. With a given number of snapshots, we compared the variance of the estimates against the CRB. Additionally, we compared the effectiveness of the MVDR technique to the CRB over varying angles of incidence and power levels.

Initially, without considering polarization and antenna element factors, we investigated isotropic antenna configuration. We observed how the increase in the dimension of the antenna (1-d, 2-d, then 3-d) would affect the performance of the MLE and MVDR techniques for DF. These numerical findings were an important step to analyze the added benefit of a 3-d volumetric array versus a 3-d planar array.

The comparison of 3 orthogonal 3-d colinear dipole arrays demonstrated the significance of the incident plane wave polarization relative to the orientation of the array itself. The benefit of having three separate arrays ensures that the main lobe of at least one array will receive the impinging wave favorably, even if the others may not (see Experiment 3).

6.2 Future Work

6.2.1 Mutual Coupling

This thesis has shown that the DF estimation methods of both MLE and MVDR could be effectively expanded to both 2-d and 3-d uniform antenna arrays using half-wave dipoles. However, one crucial aspect of volume or even planar arrays is the effect of mutual coupling

between array elements. The mutual coupling problem has been thoroughly explored in [13] and related works. The mutual coupling problem is shown to become more significant as the number of elements increases, and would likely impact DF results shown here if not properly mitigated in implementation. However, further work specific to the 3-d uniform, volume array problem would be required to account for and mitigate the mutual coupling phenomenon.

6.2.2 Ill-conditioned Matrices

One problem that was encountered throughout the conduct of this research is the problem of ill-conditioned matrices. As matrices become extremely large, the likelihood of them becoming sparse goes up dramatically, which will likely produce inaccurate or unusable results when an inverse operation is performed. Some papers, such as [14], have produced some promising results to help condition matrices for these purposes, which could be implemented in further work.

6.2.3 Phase Error

Additionally, although the noise simulated was complex Gaussian white noise, other forms of signal interference could be explored to give more accurate simulation results. Experiments could include phase errors from physical placement or displacement of antenna nodes, let alone the mutual coupling mentioned above. Phase error effects on performance should be evaluated.

All of these issues provide potential unique study and exploration into the realm of DF and angle of arrival estimation theory.

List of References

[1] T. Tuncer and B. Friedlander, *Classical And Modern Direction-Of-Arrival Estimation*. London: Academic, 2009.

[2] H. L. Van Trees, *Detection, estimation, and modulation theory. Part 4, Optimum array processing*. New York: Wiley-Interscience, 2002.

[3] A. Ferreol, C. Delestre, and P. Larzabal, "Doa estimation performances of multi-parametric music in presence of modeling errors - case of coherent multi-paths," in *2014 IEEE International Conference on Acoustics, Speech and Signal Processing (ICASSP)*. IEEE, 2014, pp. 2247–2251.

[4] W. L. Stutzman, *Antenna theory and design*, 2nd ed. New York: J. Wiley, 1998.

[5] B. Friedlander, "Sensitivity analysis of the maximum likelihood direction-finding algorithm," *IEEE Transactions on Aerospace and Electronic Systems*, vol. 26, no. 6, p. 953–968, 1990.

[6] B. Friedlander, "Maximum likelihood estimation for geolocation in the presence of multipath," in *2014 48th Asilomar Conference on Signals, Systems and Computers*, 2014, pp. 1174–1178.

[7] S. M. Kay, *Fundamentals of statistical signal processing* (Prentice Hall signal processing series). Englewood Cliffs, N.J.: Prentice-Hall PTR, 1993 - 2013.

[8] Z. L. Shuli Shi, Yougen Xu, "Block sparse representation approach to 2d doa and polarisation estimation of wideband signals using a sparse vector antenna array," *IET Radar, Sonar, and Navigation*, vol. 14, no. 12, pp. 1929–1939, 2020.

[9] J. Capon, "High-resolution frequency-wavenumber spectrum analysis," *Proceedings of the IEEE*, vol. 57, no. 8, pp. 1408–1418, 1969.

[10] M.-S. Chen and R. Liou, "Recursive mvdr for direction finding using circular arrays," in *2004 10th International Symposium on Antenna Technology and Applied Electromagnetics and URSI Conference*. IEEE, 2004, pp. 1–4.

[11] B. Friedlander, "Calibration of antenna arrays using the extended manifold," *IET Radar, Sonar, and Navigation*, vol. 14, no. 7, pp. 1001–1007, 2020.

[12] B. Friedlander, "The extended manifold for antenna arrays," *IEEE Transactions on Signal Processing*, vol. 68, pp. 493–502, 2020.

[13] J. Z. Y. H. K. Z. Yaxing Yue, Yougen Xu and Z. Liu, "Mutual coupling self-calibration for parameter estimation with vector antennas," in *2019 IEEE International Conference on Signal, Information and Data Processing (ICSIDP)*, 2019.

[14] M. A. R. Anjum and M. M. Ahmed, "A new approach for inversion of large random matrices in massive mimo systems," *PloS one*, vol. 9, no. 4, pp. e94 958–e94 958, 2014.

Initial Distribution List

1. Defense Technical Information Center
   Ft. Belvoir, Virginia

2. Dudley Knox Library
   Naval Postgraduate School
   Monterey, California